Biomaterials 320 (2025) 123256

Contents lists available at ScienceDirect

Biomaterials

journal homepage: www.elsevier.com/locate/biomaterials

Bioprinted high cell density liver model with improved hepatic metabolic functions

Ting-Yu Lu [a], Yichun Ji [b], Cheng Lyu [c], Erin Nicole Shen [c], Yazhi Sun [c], Yi Xiang [c], Tobias Meng-Saccoccio [c], Gen-Sheng Feng [b], Shaochen Chen [a,c,d,*]

[a] Program in Materials Science and Engineering, University of California San Diego, La Jolla, CA, 92093, USA
[b] Department of Pathology, Department of Molecular Biology, Moores Cancer Center, University of California San Diego, La Jolla, CA, 92093, USA
[c] Department of Chemical and Nano Engineering, University of California San Diego, La Jolla, CA, 92093, USA
[d] Department of Bioengineering, University of California San Diego, La Jolla, CA, 92093, USA

ARTICLE INFO

Keywords:
3D bioprinting
In vitro hepatic model
Primary hepatocyte
High cell density
Drug screening

ABSTRACT

In vitro liver tissue models are valuable for studying liver function, understanding liver diseases, and screening candidate drugs for toxicity and efficacy. While three-dimensional (3D) bioprinting shows promise in creating various types of functional tissues, current efforts to engineer a functional liver tissue face challenges in replicating native high cell density (HCD) and maintaining long-term cell viability. HCD is crucial for establishing the cell-cell interactions necessary to mimic the liver's metabolic and detoxification functions. However, HCD bioinks exacerbate light scattering in light-based 3D bioprinting. In this study, we incorporated iodixanol into our bioink formulation to minimize light scattering, enabling the fabrication of hepatic tissue constructs with an HCD of 8×10^7 cells/mL while maintaining high cell viability (~80 %). The printed dense hepatic tissue constructs showed enhanced cell-cell interactions, as evidenced by increased expression of E-cadherin and ZO-1. Furthermore, these constructs promoted albumin secretion, urea production, and P450 metabolic activity. Additionally, HCD hepatic tissue inactivated the YAP/TAZ pathway via cell-cell interactions, preserving primary hepatocyte functions. Further screening revealed that hepatocytes in the dense model were more sensitive to drug treatments than those in a lower-density hepatic model, highlighting the importance of HCD in recapitulating the physiological drug responses. Overall, our approach represents a significant advancement in liver tissue engineering, providing a promising platform for the development of physiologically relevant *in vitro* liver models for drug screening and toxicity testing.

1. Introduction

The liver serves a crucial function in synthesizing essential proteins and metabolizing xenobiotics. It follows that liver dysfunction is closely linked to disease development and drug-induced toxicity. Numerous genetic and metabolic disorders can affect the liver, such as fibrosis and cirrhosis [1,2]. Given the liver's central role in xenobiotic metabolism, parenchymal cell cultures serve as essential *in vitro* models for studying detoxification processes [3]. Consequently, extensive efforts have been made to develop *in vitro* liver models, both for investigation of pathophysiological mechanisms and as accessible alternatives to animal models during drug hepatotoxicity screenings [4,5]. Primary hepatocyte cultures have emerged as a promising tool for detecting general or liver-specific toxicity and evaluating species-specific drug effects [6]. While various approaches for isolating and cultivating primary hepatocytes have been successful, their utility is often limited by challenges in maintaining viability and metabolic function [7]. In traditional 2D cultures, primary hepatocytes typically cannot survive beyond 2 weeks, quickly losing their differentiated state and metabolic functions. In contrast, *in vitro* 3D cultures of primary hepatocytes have shown considerable promise in maintaining hepatocyte viability, stable phenotype, morphology, and metabolic functions over extended culture periods [8,9]. Recent studies have demonstrated that incorporating supportive stromal cells and non-parenchymal cells into co-culture systems significantly enhances the stability, maturation and longevity of primary hepatocyte cultures [10,11]. These co-culture approaches

* Corresponding author. Program in Materials Science and Engineering, Department of Chemical and Nano Engineering, Department of Bioengineering, University of California San Diego, La Jolla, CA, 92093, USA.
E-mail address: shc064@ucsd.edu (S. Chen).

https://doi.org/10.1016/j.biomaterials.2025.123256
Received 16 November 2024; Received in revised form 14 February 2025; Accepted 10 March 2025
Available online 11 March 2025

help maintain hepatocyte-specific functions by providing essential cell-cell and cell-matrix interactions, which are crucial for mimicking the *in vivo* liver microenvironment. Inclusion of these supportive cells in 3D models further improves the physiological relevance of *in vitro* systems for studying liver response, xenobiotic biotransformation and drug-induced hepatotoxicity [12]. This shift towards more advanced culture models underscores the ongoing effort to develop physiologically relevant platforms for drug development and toxicology studies.

Native human tissues typically exhibit a cell density ranging from 1 to 2 billion cells/mL [13]. However, traditional bioink formulations generally have cell densities in the range of (0.1–10) $\times$ 10^6 cells/mL, which is orders of magnitude lower than the levels found in native tissues like the liver [14–18]. The use of low density bioinks in 3D bioprinting methods has arisen because higher cell densities significantly reduce bioink printability and cell viability [19,20]. Yet, primary hepatocytes thrive in high cell density (HCD) environments, which promote enhanced cell-cell and cell-extracellular matrix (ECM) interactions necessary for maintaining cellular function and phenotype [21–23]. In contrast, these interactions are limited in traditional 2D cultures. HCD is essential for accurately recapitulating various pathological tissue states, such as regeneration and function, in which perturbed cell-cell and cell-ECM interactions play a central role. Therefore, achieving HCD bioinks is crucial for the development of more physiologically relevant tissue models and enhancing our understanding of tissue pathology [24].

Biofabrication technologies, such as digital light processing (DLP)-based 3D bioprinting, play a critical role in tissue engineering by facilitating the programmed assembly of cells into intricate 3D geometries with high resolution, cell viability, and speed [25–28]. DLP bioprinting works by projecting light patterns onto photopolymerizable bioinks, triggering polymer crosslinking in precise geometries, distinguishing it from extrusion-based bioprinting methods [29]. While extrusion-based printing can achieve a nominal resolution of 50 μm and light-based printing can reach several microns, achieving finer features requires precisely optimizing fabrication conditions, typically by using materials that exhibit low-biocompatibility, high photosensitivity, and poor cell encapsulation [30,31]. Researchers have developed several strategies to create high-resolution bioprinted hepatocyte models [32–35]. However, these studies are typically limited to low cell densities ($\leq$20 million cells/mL), and even so, use of cell-laden bioinks in actual bioprinting applications often causes print resolution to significantly diminish from ideal outcomes. To increase cell density, there is growing interest in using cellular spheroids to engineer functional hepatic tissues with the requisite HCD [36–39]. Increased cell density or the use of spheroids in bioink necessitates a larger nozzle tip for extrusion-based 3D bioprinting, which lowers print resolution [40]. Additionally, hepatocytes, being larger cells with a diameter of 20–30 μm, face significant shear forces during extrusion, leading to impaired cell viability [41]. Although DLP-based 3D bioprinting is free from extrusion-based shearing concerns, light-based technologies have primarily been designed to process cells embedded within hydrogels, limiting cell-cell interactions and resulting in low cell density (LCD) constructs [42]. Attempts to increase cell density in hydrogel-based bioinks typically result in severe cell-induced light scattering, causing errant photopolymerization that deforms the print structure [43,44]. In summary, simultaneously achieving HCD ($\geq$20 million cells/ml), high cell viability ($\geq$80 %), and finely resolved hepatic tissue constructs remains a significant challenge.

Our previous study demonstrated that biocompatible iodixanol (IDX) enables precise tuning of optical bioink properties, effectively reducing light scattering by matching the refractive index of the bioink components. This minimization of scattering enhances light penetration and focal precision, ultimately improving printing quality at HCD [19]. This allowed us to achieve micron-scale resolution prints using a high density of cells encapsulated in natural hydrogels [17,38]. In this study, we combined methacrylated gelatin (GelMA) with IDX to produce an HCD liver model using DLP bioprinting (Fig. 1a). We bioprinted hepatic tissues composed of primary mouse hepatocytes (PMH) with high cell viability, facilitating accelerated tissue remodeling due to robust cell-cell interactions. Markers of cell-cell interaction, including albumin secretion, urea production, and CYP450, were highly expressed. By assessing transcriptome profiles, liver-specific markers, and metabolic gene expression, we demonstrated that the HCD hepatic model can recapitulate and maintain hepatic function. Moreover, the HCD hepatic tissue creates a confluent cell environment that upregulates cell adhesive and tight junction gene expression, leading to the inactivation of the YAP/TAZ pathway through cell-cell interactions, thereby preserving primary hepatocyte function [45]. Finally, based on this HCD model, we investigated the metabolic transformation of various drugs via dynamic culture systems, utilizing CYP activity measurement, mass spectrometry analysis, and drug cytotoxicity assays to elucidate metabolic enzyme functions in hepatic tissue.

2. Method

2.1. GelMA synthesis

Gelatin methacrylate (GelMA) was synthesized from type A gelatin (Cat. #G2500, Sigma-Aldrich) and methacrylic anhydride (MA, Cat. #276685, Sigma Aldrich) in a 0.25 M carbonate-bicarbonate (CB)

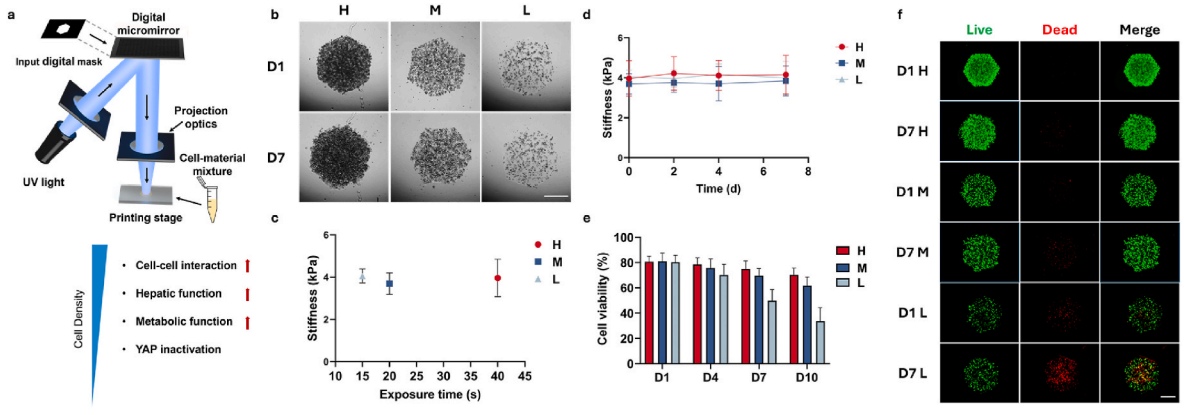

Fig. 1. Fabrication of an HCD liver model. (a) Schematic illustration of the DLP-based bioprinting process for the HCD liver model. (b) 3D bioprinted constructs of different hepatocyte densities on day 1 and day 7. (c) Plot showing the relationship between scaffold compressive modulus and print exposure time for different cell densities. (d) Quantitative plot showing the compressive moduli of cell-embedded scaffolds over 7 days. (e) Cell viability measurement of different hepatocyte densities at various time points. (f) Live/dead staining of different hepatocyte densities on day 1 and day 7. Scale bar: 500 μm.

buffer, following a previously described method [46–48]. In brief, a 10 % (w/v) gelatin solution in the CB buffer was allowed to react with MA at a MA/gelatin ratio of 0.085 mL/g for 1 h at 50 °C. The reaction was then quenched by adjusting the pH to 7.4. The resulting mixture was dialyzed using 12–14 kDa cutoff dialysis tubing against MilliQ water for 3 days and subsequently lyophilized for future use. The degree of functionalization (DoF) of GelMA was quantified by ^{1}H NMR (Fig. S1).

2.2. Primary mouse hepatocyte isolation

All research conducted in this study adhered to approved Institutional Review Board (IRB) protocols at the University of California, San Diego (UCSD). Furthermore, all animal work associated with this research received approval from UCSD's IRB. The animal work was conducted in strict accordance with the guidelines outlined by the Institutional Animal Care and Use Committee (IACUC), ensuring ethical and humane treatment of animals in our research. Primary mouse hepatocytes (PMH) were isolated from 8- to 10-week-old mice using a two-step collagenase digestion method. In brief, mice were euthanized with CO2, and the abdomen was carefully opened to expose the portal vein and inferior vena cava. Perfusion buffer was introduced into the portal vein, and the vena cava was severed. The liver was perfused with the buffer, which contained collagenase H (Cat. #11074032001, Roche) and HEPES (Cat. #15630080, Gibco), at a rate of approximately 10 mL/min. The liver was then carefully excised and washed through a 100 μm filter. Hepatocytes were isolated by gradient centrifugation. The resulting single-cell suspensions were washed with DPBS, and the cells were resuspended in hepatocyte culture medium (HCM; Cat #CC-3198, Lonza) containing all supplied supplements along with 1 % penicillin–streptomycin.

2.3. 3D bioprinting of the PMH models

GelMA and lithium phenyl-2,4,6-trimethylbenzoylphosphinate (LAP, Cat. #85073-19-4, Sigma-Aldrich) were dissolved in Dulbecco's phosphate-buffered saline (DPBS, Cat. #14190144, Gibco) to create stock solutions of 20 % (w/v) and 4 % (w/v), respectively. To prepare the prepolymer solutions, all stock solutions were warmed to 37 °C prior to use. The final prepolymer solution was formulated by mixing 12 % GelMA, 0.4 % LAP, 60 % iodixanol (IDX), and DPBS as the solvent. This solution was maintained at 37 °C on a heat block and was covered with aluminum foil to prevent premature photopolymerization. Micro-tissue constructs were bioprinted using a previously reported method [49,50]. In brief, an in-house micro-continuous optical printing (μCOP) system was employed, and polydimethylsiloxane (PDMS) spacers were utilized to control sample thickness. A PDMS-coated coverslip was placed on top of the solution and spacers to create a smooth surface. The solution was then exposed to UV light using a projected light pattern. For bioink preparation, the prepolymer solution was combined with the cell suspension at a 1:1 ratio, resulting in final cell densities denoted high (80 million cells/mL), medium (20 million cells/mL), or low (5 million cells/mL), depending on the printing requirements. The cell-laden bioink was then carefully loaded onto the printer stage for use. After loading, bioink was polymerized over an appropriate exposure time using 365 nm light. Following printing, warmed DPBS was used to wash away the excess bioink-cell solution.

2.4. Mechanical testing

A mechanical tester ("MicroSquisher," CellScale) was employed to measure the compressive modulus of the printed samples [51]. For each cell-bioink mixture, pillars with a diameter and height of 500 μm were printed using the same setup used for different cell density liver models. The pillars were stored at 37 °C prior to taking measurements to mimic physiological culture conditions. While taking measurements with the MicroSquisher, stainless steel beams and platens were used to consecutively compress the constructs by10 % of their original height for three cycles. Data from the last of the three measurements was used for analysis, and the compressive modulus was calculated using customized MATLAB scripts to analyze the force and displacement data [52].

2.5. Cell viability analysis

Cell viability analysis was conducted on days 1, 3, 7, and 10 following bioprinting with PMHs. To conduct live/dead staining, samples were washed twice with DPBS after removing the culture medium. Samples were subsequently incubated with a solution containing 1 μM calcein AM (live cell stain, Cat. #C3099, Invitrogen) and 2 μM ethidium homodimer-1 (dead cell stain, Cat. #P3566, Invitrogen) at room temperature for 30 min [53]. Image acquisition using a Leica DMI 6000B microscope (Leica Microsystems) was immediately performed after incubation. Cell viability was also quantified using the CCK-8 assay (Cat. #K1018, ApexBio) using four biological replicates for each condition. At designated time points, the samples were washed with DPBS, incubated with 500 μL of fresh media with 10 % CCK-8 reagent under regular incubation conditions for 60 min. After incubation, 200 μL of the supernatant was collected from each sample, and its absorbance was measured at 450 nm using a Tecan Infinite 200 PRO.

2.6. Immunofluorescence staining

Bioprinted constructs were rinsed with Dulbecco's phosphate-buffered saline (DPBS) three times and fixed with 4 % paraformaldehyde for 1 h at room temperature. The block/permeabilization solution was prepared by dissolving 5 % (w/v) bovine serum albumin (BSA, SKU#700-101P, GeminiBio) and 0.1 % Triton X-100 (Cat. #H5141, Promega) in DPBS. The solution was filtered after complete dissolution. Fixed samples were blocked/permeabilized for 1 h at room temperature on a shaker at 100 rpm. Primary antibodies (Table S3) were diluted in Cell Staining Buffer (Biolegend), and the samples were incubated in the primary antibody solution overnight at 4 °C. Subsequently, samples were rinsed three times with DPBS and incubated with secondary antibodies and DAPI Table S3) in the dark for 1 h at room temperature on a shaker. After the secondary incubation, samples were rinsed three times with DPBS. The stained samples were then imaged using a Leica SP8 fluorescence confocal microscope.

2.7. Flow cytometry

To analyze different PMH densities in the bioprinted construct, cells were collected by degrading the collagen matrix with collagenase type I (2 mg/mL, Cat. #17100-017, GIBCO) at 37 °C for 30 min. The collected cells were washed, fixed, and blocked using the Cytofix/Cytoperm kit (Cat. 554724, BD Biosciences), followed by additional blocking with TruStain FcX PLUS (Cat. #156603, Biolegend). Primary antibodies (refer to Table S3) were used for cell staining at 4 °C for 30 min. After three washes, cells were stained with secondary antibodies. Flow cytometry was performed using a BD LSRFortessa SORP. All data were analyzed using FlowJo v10.

2.8. Cytochrome P450 activity

Cytochrome P450 activity was assessed using a P450-Glo 2C9/3A4 Assay Kit (Promega), and the luminescence activity was measured with a luminometer in accordance with the manufacturer's instructions. 3D printed liver models were washed in DPBS before being incubated with reagent for 1 h at 37 °C. After washing, 25 μL of supernatant was transferred into the wells of a white 96-well plate, mixed with 25 μL of the detection reagent, and incubated for 20 min in the dark at room temperature. The plate was transferred into a multimode microplate reader and luminescence was measured using a 1 s integration time. The

background signal of the assay (no cells) was subtracted from measurements of the cell cultures.

2.9. Albumin and urea secretion quantification

The culture supernatants were collected from samples at various time points and stored at −80 °C before analysis. Urea production quantification was performed using a QuantiChrom™ BCG Albumin Assay Kit and QuantiChrom™ urea assay kit (BioAssay Systems) according to the manufacturer's instructions. The amounts of albumin and urea secreted were calculated based on standard curves from each experiment, followed by normalization to the viable cell population, ensuring accurate representation of secretion data relative to the actual number of active cells within the constructs.

2.10. RNA isolation and quantitative real-time reverse-transcription PCR (qRT-PCR)

RNA extraction was conducted using TRIzol reagent (Life Technologies). To obtain sufficient RNA from the bioprinted liver constructs, 10 samples were combined and all RNA was extracted in unison. In brief, bioprinted liver constructs were incubated with TRIzol reagent followed by purification using a spin-column method with Direct-zol RNA Microprep (Cat. #R2060, Zymo Research), and the RNA concentration was evaluated using a Tecan plate reader after resuspending RNAs in RNase-free water. The RNA samples were immediately stored at −80 °C. For qRT-PCR, 200 ng of RNA was first converted to cDNA using the First Strand cDNA Synthesis Kit (Cat. #E6300S, New England BioLabs). Subsequently, qRT-PCR was performed using the Luna® Universal qPCR Master Mix (Cat. #M3003S, New England BioLabs) and the Quantstudio 3 qRT-PCR system. The relative quantification of specific genes was determined by normalizing the threshold cycle (Ct) values against the housekeeping gene. The forward and reverse primers were purchased from Integrated DNA Technologies, and primer sequences are listed in Table S4.

2.11. RNA sequencing and data analysis

RNA-seq was performed on the following samples: (1) HCD and (2) medium cell density (MCD) groups. Total RNA was isolated by the extraction reagent TRIzol introduced above. The concentration of the RNA library was diluted to 1 ng/μL according to the measurement by Qubit® RNA Assay Kit in Qubit® 3.0 and the insert size was assessed by the Agilent Bioanalyzer 2100 system (Agilent Technologies, CA, USA). Cluster generation and sequencing were conducted with a Novaseq 6000 S4 platform. Around 40 million to 60 million total reads were obtained for each sample. RNA quality evaluation and sequencing were performed by Novogen Inc. For three biological replicates of each condition. For the analysis of Differentially Expressed Genes (DEGs), HISAT2 v2.0.5 was used to map sequence reads to the *Mus musculus* transcriptome (*Mus musculus*.mm39). Gene expression was evaluated by Fragments Per Kilobase Million Mapped Reads (FPKM) values by using HTseq-count (v.0.6.0). DESeq2 (v.1.20.0) was used to identify DEGs with a fold change cut-off threshold $\geq$1 and false discovery rate (FDR)-adjusted p-value $<$0.05. Typical DEGs related to the specific hepatic function and liver fibrosis were used for plotting heatmaps. Fold change of gene expression was normalized through logarithmic transformation at a base number of 2 as log2-FoldChange. Heatmaps of log2-FoldChange were plotted via SRplot heatmap [54].

2.12. Liver constructs within a microfluidic chip for dynamic culture

The uncoated μ-Slide III 3D Perfusion chip (Ibidi, Cat. No: 80376) was selected for this study. Microfluidic experiments were performed using hepatocyte culture medium as previous described. Chips were pre-warmed for about 1 h before loading. The 5 mm coverslip with a printed liver model was placed on the chip and 30 mL of culture medium was added. Lastly, the chip was sealed with an adhesive Ibidi Polymer Coverslip to prevent bubble formation. The dynamic culture condition was performed at a flow rate of 0.1 mL/min and a temperature of 37 °C.

2.13. CYP induction

To assess CYP induction potential, the CYP activity levels in rifampicin-treated and untreated samples were measured using the qRT-PCR and P450-Glo CYP Assay Kit as described above. The cells were treated with rifampicin (20 and 40 μM with a total of 0.1 % DMSO in culture medium; Sigma-Aldrich) for 2 days, while non-treated samples (with a total of 0.1 % DMSO in culture medium; Life Technologies) were used as controls for comparison. Relative quantification was performed using a standard curve, and the values were normalized against the input determined for the housekeeping gene GAPDH.

2.14. Mass spectrometry (MS) analysis for quantification of cellular drug metabolism

Phenotype-specific drug response of individual groups was assessed by subjecting cultures to a mixture of known substrates for the Cytochrome P450 system (Table S1). The collected medium was vortexed with methanol in a 1:2 vol ratio, and then the mixture was centrifuged at 10,000 rpm for 10 min to facilitate desalination and deproteinization. Metabolite concentrations were then measured via high performance liquid chromatography separation paired with tandem mass spectrometry detection on a Micromass Quattro Ultima triple quadrupole mass spectrometer. The supernatant was diluted with ultrapure water in a 1:8 vol ratio and loaded onto a C18 column with an injection volume of 2 μL. Separation of drugs and their metabolites was performed on C18 column at a flow rate of 3 μL/min and a temperature of 40 °C. Compound detection was based on the mass numbers detailed in Table S1. Based on the quantified metabolite concentrations, metabolic conversion rates were then estimated.

2.15. Drug response assessment

To evaluate the performance of the HCD liver model as a drug screening platform, a cytotoxicity assay was conducted on the chip. For comparison, an MCD model was also used. Both models were supplemented with increasing concentrations of Cyclophosphamide (CPA, Cat. #6055-19-2, Sigma) (5, 10, 50, 100, and 500 μg/mL). Viability was assessed after 24 h using a CCK-8 test. Absorbance results at a wavelength of 450 nm were recorded for each concentration in each model.

2.16. Statistical analysis

Sample populations were compared using a *t*-test or one-way ANOVA performed with GraphPad Prism (GraphPad Software). *$p < 0.05$, **$p < 0.01$ and ***$p < 0.001$ were used as the thresholds for statistical significance. Data points on the graphs represent mean values with error bars representing SEM.

3. Result and discussion

3.1. HCD bioprinted liver models with IDX exhibit sustained high cell viability and tunable mechanical stiffness

To understand the effect of cell density on PMH function, we selected three cell densities: 5, 20, and 80 million cells/mL, representing low (L), middle (M), and high (H) density groups, respectively (Fig. 1b).

Although low-density levels are commonly used to create functional constructs in many studies, we hypothesized that such densities may be insufficient for generating highly functional tissue. We previously defined an HCD bioprinting protocol by incorporating IDX into the

bioink, allowing the HCD and MCD groups to be printed in the desired structure with minimal light scattering [19]. Our current study presents quantitative data demonstrating how varied IDX concentrations alter the refractive index of the bioink, allowing it to closely match that of the cytoplasm (1.36–1.39) [55–57]. As shown in Fig. S2, we observed a linear increase in refractive index with increasing IDX concentrations up to 35 %. This precise control is particularly useful for minimizing light scattering, especially in larger HCD constructs. While previous studies have used IDX for scattering correction, our data offers a more precise method for refractive index tuning, enabling critical enhancements in printability and optical transparency for light-based bioprinting methods and engineered hepatocyte models. Our findings indicate that 30 % IDX provides an optimal balance between refractive index tuning and reduced scattering, allowing for improved bioprinting fidelity. Numerous factors impact cell viability in the DLP process; however, our results showed only a 3.85 % decrease in viability after printing with IDX, demonstrating the reliability of our method (Fig. S3). Emerging evidence suggests that mechanical stiffness, when mimicking native tissue environments, can impact hepatic function [58]. To achieve consistent mechanical stiffness across constructs with different cell densities, we adjusted the printing parameters by regionally varying exposure time, allowing for uniform modulation of mechanical properties within the same construct. Mechanical testing of the 6 % (wt/vol) GelMA-based constructs demonstrated a positive linear relationship between the stiffness and the exposure time (Fig. S4). Based on these findings, we selected a photopolymerized matrix stiffness similar to that of healthy liver tissue to support PMH (Fig. 1c). Specifically, exposure times of 15, 20, and 40 s were chosen to produce scaffolds with identical stiffness (4 kPa) for the L, M, and H cell density groups, respectively. Cell-embedded scaffolds were fabricated under these conditions, and stiffness measurements were performed to determine scaffold stability over a 7-day culture period. The changes in stiffness over 7 days were not significant for all three conditions in cell-embedded scaffolds (Fig. 1d). Post-printing, cell viability and live/dead staining demonstrated that HCD bioprinting of PMHs achieved high viability (~80 %) over the 7-day culture period, while LCD PMH scaffolds exhibited lower viability (~50 %). This indicates that HCD bioprinting can sustain cell viability over an extended duration, compared to hepatocytes cultured in an LCD (5 million cells/mL) format (Fig. 1e–f).

3.2. *HCD enables greater intercellular interactions and metabolic function in the hepatic model*

To better understand cellular activity after bioprinting, we characterized intercellular interactions and metabolic hepatocyte functions. Our hypothesis posits that hepatocytes in HCD environments more readily form cell aggregates, which have been shown to enhance cell-cell interactions, cell viability, and metabolic function for prolonged periods due to improved retention of *in vivo* hepatic morphology [59–61]. To study PMH in different cell density groups, we performed immunofluorescent staining for (1) E-cadherin (adhesive junction), an epithelial marker that had been shown to protect primary hepatocytes from apoptosis [62]; (2) ZO-1 (tight junction); and (3) albumin, an indicator of hepatic function (Fig. 2a–b and Fig. S6). Then, we measured the size of cellular aggregates, observing larger aggregates in the HCD group after 7 days of culture (Fig. 2a and Fig. S5). In contrast, only a few small aggregates formed in the MCD group, and scarcely any formed in the LCD group. HCD cultures after 7 days showed strong positive staining for

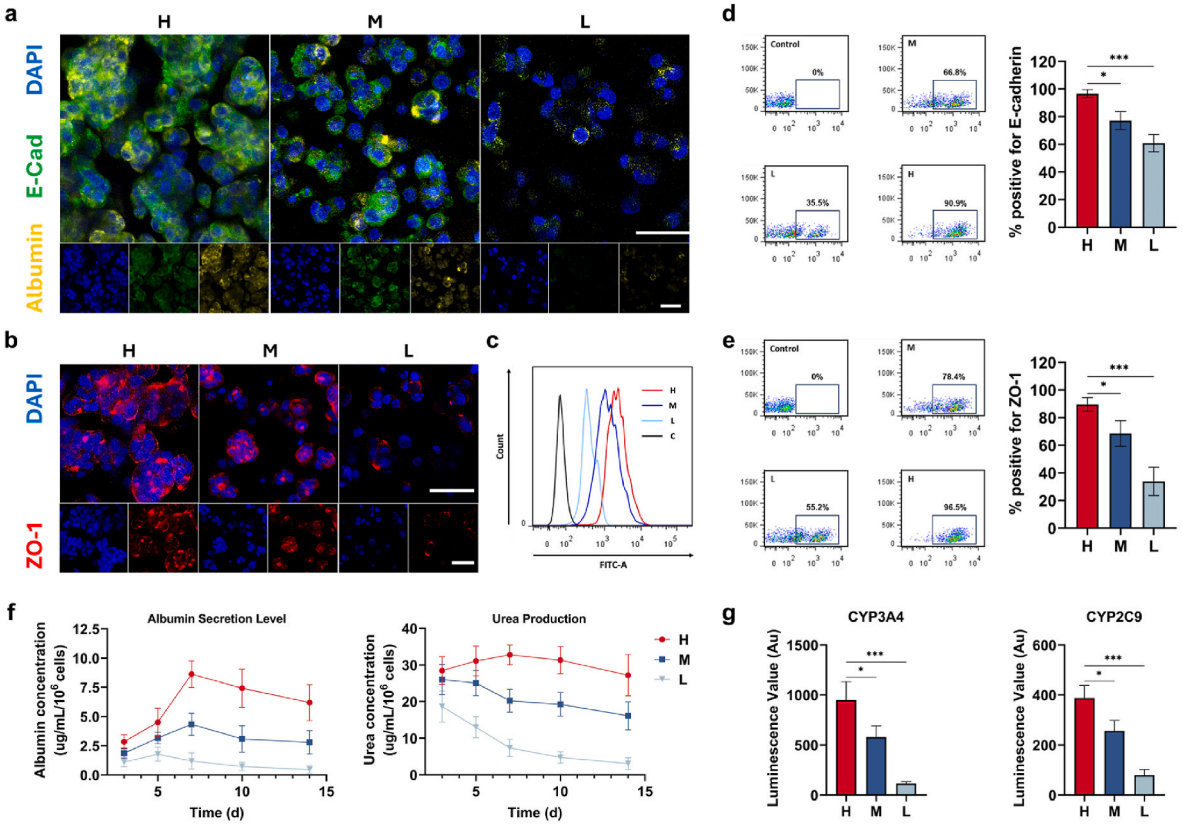

Fig. 2. Bioprinted HCD hepatic model enhances cell-cell interaction and maintains hepatic functions. (a) Confocal microscopy images showing E-cadherin formation and albumin secretion and (b) ZO-1 formation in different PMH cell density groups (H, M, L). Scale bar 50 μm. (c) Flow cytometry analysis of intracellular albumin production. Evaluation of the expression of % positive cells and quantitative analysis of (d) E-cadherin and (e) ZO-1 by flow cytometry. (f) Albumin and urea secretion by hepatocytes across H, M, and L densities over time. (g) CYP3A4 and CYP2C9 activity in different density groups at day 7. Error bars represent mean ± s. d. ***p < 0.001, **p < 0.01 and *p < 0.05.

all three markers, indicating functional spheroid formation. Quantifying fluorescent intensity in immunofluorescent images showed significant improvements of cell-cell interaction and albumin secretion in HCD compared to MCD and LCD. To further investigate cellular function, we used flow cytometry to measure intracellular albumin expression, which was found to be significantly higher in HCD cultures (Fig. 2c and Fig. S7). We also observed notable changes in the expression of E-cadherin and ZO-1 between the different cell density groups (Fig. 2d–e). Next, we compared anabolic and catabolic function of the PMHs across different models. Albumin secretion levels were monitored over a 2-week period, given its role in maintaining oncotic pressure in the body (Fig. 2f). Although albumin secretion declined in all three models after their respective peaks, PMHs in HCD maintained the highest level of albumin secretion 7 days after bioprinting. Similarly, we measured urea production over time, as it is indicative of the hepatocytes' ability to break down amino acids. PMHs in HCD consistently exhibited higher urea production compared to those in MCD and LCD environments. The metabolic activity of hepatocytes, which largely depends on cytochrome P450 enzyme activity, was also assessed. Specifically, we measured the activities of CYP2C9 and CYP3A4 enzymes and found that both were significantly increased in HCD cultures (Fig. 2g).

3.3. *HCD model drives transcriptional reprogramming to enhance hepatic gene expression and function*

The aforementioned results regarding cell viability, cell-cell interaction, and liver metabolic function showed that these cellular benchmarks dropped significantly after 7 days of culture in LCD conditions. This demonstrates that withincurrent cell density ranges (1–10 million cells/mL), maintaining proper primary hepatocyte function is extremely challenging [14]. To further investigate the differences in cellular function under different cell density conditions, we performed global transcriptome profiling. RNA was extracted from PMHs cultured in bioprinted constructs and isolated from both HCD and MCD conditions. RNA sequencing (RNAseq) was then conducted to evaluate gene expression differences and identify major signaling pathways that were differentially regulated between the two conditions.

We first assessed the overall similarity between the transcriptional profiles of hepatocytes in HCD and MCD conditions using Spearman rank correlation. The analysis yielded a correlation coefficient of 0.77, indicating a moderate degree of difference between the two conditions (Fig. 3a). Principal component analysis (PCA) was conducted to visualize the variance in gene expression between HCD and MCD. The PCA plot showed that the HCD culture had a markedly different transcriptional profile compared to the MCD condition, highlighting the significant impact of cell density on gene expression (Fig. S8). To identify specific genes that were differentially expressed between the HCD and MCD conditions, we generated a volcano plot, which revealed a total of 7363 differentially expressed genes (DEGs) with a | log2 (fold change) | and Q value < 0.05. These DEGs were labeled on the map, illustrating the extensive transcriptional reprogramming induced by the different cell density environments (Fig. 3b).

We then analyzed the liver-specific gene expression (LiGEP; Fig. 3c) to validate our HCD liver model's metabolic function [63]. The homologous mouse LiGEP heat maps revealed an upregulation in gene expression profiles under HCD conditions on day 7, indicating good maintenance of liver function in HCD cultures. These results demonstrated effective preservation of PMH functionality under our HCD bioprinting conditions. As represented by the top 10 GO terms of DEGs (H vs M) in Fig. 3d, the upregulated GO terms were primarily associated with metabolic and biosynthetic processes, including cytochrome P450, steroid, and retinol metabolism, as well as cell-cell communications and interactions, such as cell junction organization and integrin signaling. These findings highlight the enhanced metabolic activity and robust cell-cell interactions in HCD cultures. Down-regulated DEGs largely pertained to cell division and cell cycle processes. While this suggests reduced cell proliferation under HCD conditions, this reduction also indicates that hepatocytes in HCD maintain normal physiological functions without initiating cell division and repair programs, which is consistent with a stable hepatic phenotype.

Genes related to chemokine response were downregulated in HCD compared to MCD. This suggests that PMHs experience less stress in HCD conditions than MCD, which may contribute to their improved functionality and viability. To further validate the hepatic phenotype of

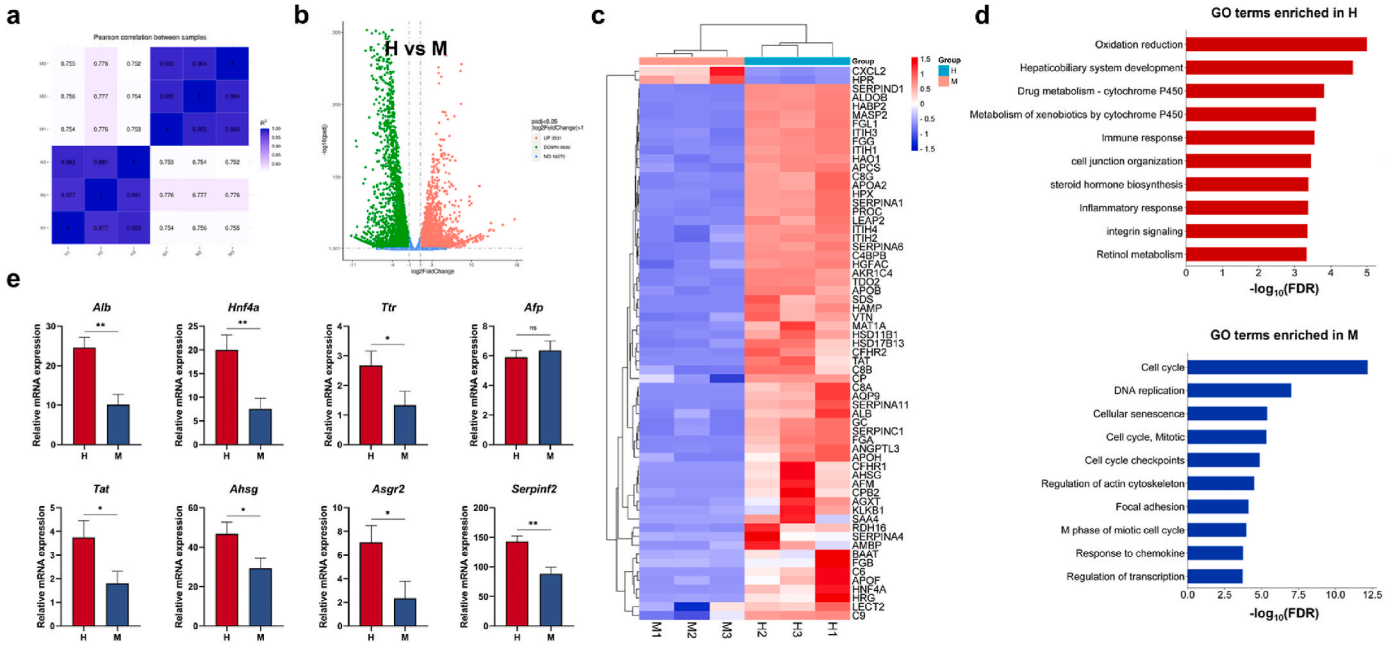

Fig. 3. Transcriptomic analysis of PMH cultivated in HCD and MCD models. (a) Global gene expression correlation study of PMHs. (b) Volcano plot of statistically significant differentially expressed genes at $Q < 0.05$ identified from RNA-Seq libraries of PMHs. (c) Heatmap (−log2 z-scores) displaying the expression of homologous mouse LiGEP genes. (d) Top 10 GO terms of up-regulated (top) and down-regulated (bottom) DEGs. (e) Plots showing PMH gene expressionin high and medium culture densities. Error bars represent mean ± s.d. $^*p < 0.05$ and $^{**}p < 0.01$.

PMHs in HCD and MCD conditions, we performed qRT-PCR on a panel of hepatocyte markers including critical hepatic transcription factors (*Hnf4a*, *Ttr*, and *Tat*), key serum proteins (*Alb* and *Ahsg*), serum glycoprotein homeostasis mediator *Asgr2*, and *Serpinf2* which encodes alpha 2-antiplasmin and regulates the blood clotting pathway (Fig. 3e). The expression of all these genes was elevated in HCD PMHs compared to MCD. This elevation indicates better maintenance of hepatic functions in HCD conditions. The expression levels of the fetal hepatic marker *AFP* were not significantly different between the two conditions, suggesting that PMHs in both groups maintained a mature state.

3.4. Measuring xenobiotic metabolism in the HCD model

To further evaluate liver function within HCD constructs, we

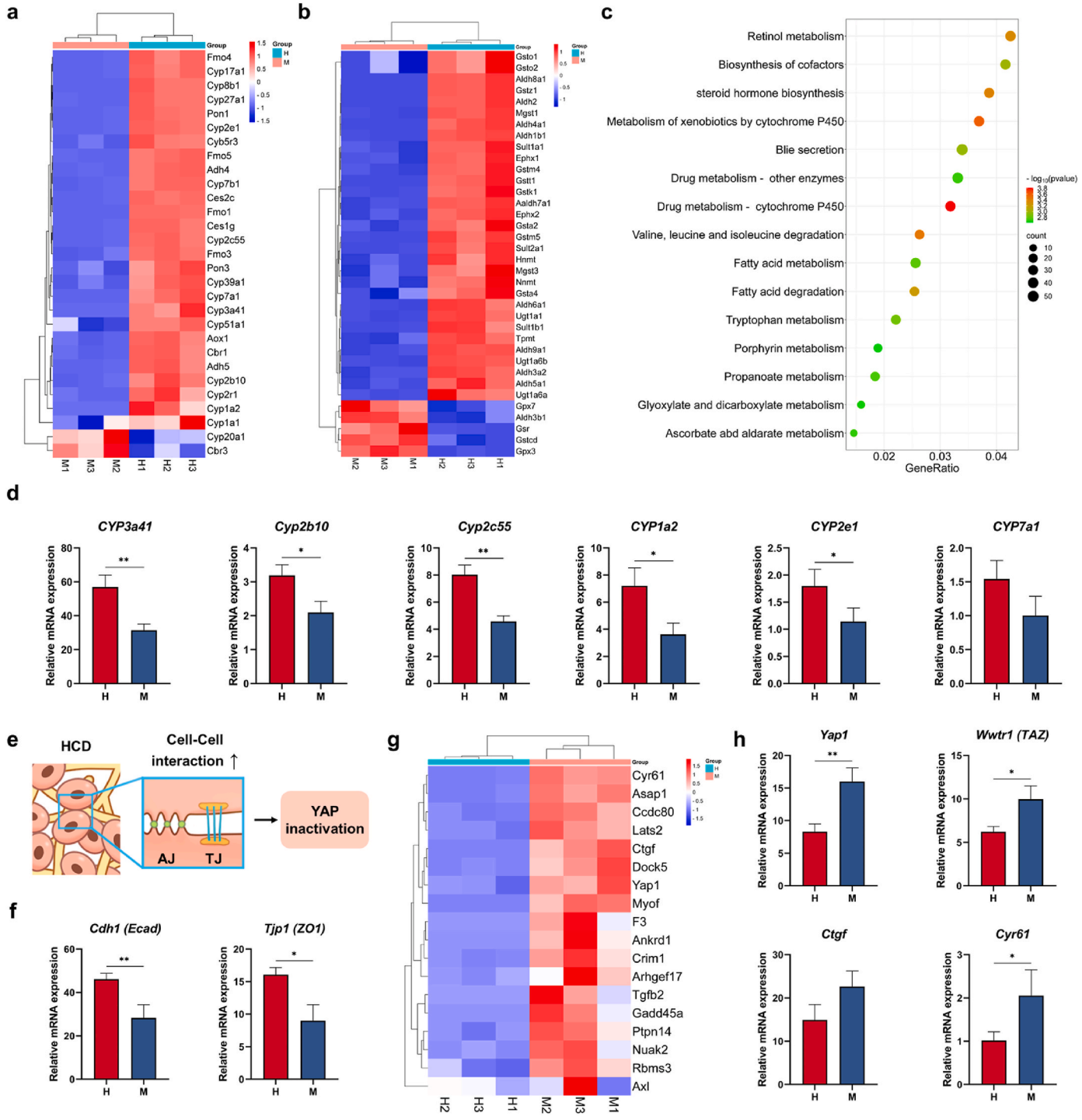

Fig. 4. Recapitulating the physiological liver environment maintains hepatocyte enzyme functions and inactive YAP status in the HCD model. (a) Heatmap displaying the expression of phase I enzyme and (b) phase II enzyme genes (−log2 z-scores) in the HCD and MCD liver models. (c) KEGG pathway analyses for the differentially expressed genes between HCD and MCD liver models based on RNA-seq. (d) Plots showing cytochrome P450 related CYP gene expression fold change of PMH for HCD and MCD. (e) A schematic diagram of AJs protein E-cadherin and TJs protein ZO-1 by which mechanical cues inhibit the activities of YAP/TAZ. (f) Plots showing AJs and TJs gene expression fold change of PMH. (g) Heat map showing up-regulation of global YAP signature genes in the MCD model relative to hepatocytes from the HCD model. (h) Plots showing YAP related gene expression fold change of PMH. Error bars represent mean ± s.d. *P < 0.05 and **p < 0.01.

analyzed the expression of genes associated with xenobiotic metabolism. This analysis included a focus on both phase I and phase II metabolism enzymes as well as hepatic transporters. Heatmap analysis of phase I metabolism genes at day 7 (Fig. 4a) revealed significant up-regulation in HCD constructs compared to MCD ones. Notably, genes related to the cytochrome P450 (CYP) enzyme family—such as *Cyp3a41*, *Cyp2c55*, *Cyp2b10*, and *CYP1a2*—were markedly elevated in HCD, indicating enhanced metabolic enzyme functions in PMHs. As key components of the phase I xenobiotic metabolism pathway, CYP enzymes play a crucial role in the bioactivation of many drugs and contaminants. We then compared the mRNA expression levels of phase II metabolism enzymes and hepatic transporters (Fig. 4b and Fig. S9), finding generally higher expression in HCD compared to MCD. Furthermore, gene ontology (GO) analysis revealed that the functional enhancements in HCD were associated with multiple metabolic pathways, including xenobiotic metabolism by cytochrome P450, drug metabolism-cytochrome P450, and retinol metabolism (Fig. 4c). Cytochrome P450 pathways are of particular interest due to their crucial role in the metabolism of many medicines and endogenous compounds, underscoring the importance of liver models for drug testing. To substantiate our findings, we conducted qRT-PCR analysis on the expression of key cytochrome P450 (CYP) enzymes involved in drug metabolism (Fig. 4d). The following CYP genes were examined: *Cyp3a41*, *Cyp2c55*, *Cyp2b10*, *Cyp1a2*, *Cyp2e1*, and *Cyp7a1*. These enzymes are collectively responsible for approximately 60 % of drug oxidation processes [64]. PMHs in the HCD model exhibited significantly elevated levels of *CYP3a41* gene expression compared to the MCD model. Given that CYP3A4 is the most prevalent CYP enzyme and is estimated to be involved in the metabolism of around half of the drugs currently in clinical use [65], its increased expression underscores the enhanced metabolic capacity of the HCD constructs. The remaining five CYP enzymes also demonstrated higher expression in HCD compared to MCD. The qRT-PCR results confirmed that the HCD liver constructs significantly enhance the expression of major CYP enzymes compared to MCD. This elevated expression aligns with the metabolic functions observed in our RNA-seq results, further validating the HCD model as a highly functional and physiologically relevant platform for drug screening and toxicity testing. By ensuring high expression levels of critical CYP enzymes, these constructs provide a robust system for the evaluation of drug metabolism, potentially improving the predictive accuracy of *in vitro* liver models in pharmaceutical development.

We also performed RNA-Seq data analyses to compare freshly isolated human hepatocyte (FH). A total of 163 upregulated and 122 downregulated genes were commonly shared between HCD and MCD compared to FH (Fig. S10a). While certain liver-specific (LiGEP) and phase I enzyme genes were upregulated in HCD relative to MCD, overall gene expression in HCD remained lower than in FH (Figs. S10b and c). Furthermore, KEGG pathway analysis further revealed that FH exhibited greater metabolic activity than HCD, particularly in xenobiotic metabolism, drug metabolism via cytochrome P450, and retinol metabolism (Fig. S10d). These findings indicate that despite enhanced hepatic function in HCD compared to MCD, our HCD model still needs to be improved on the metabolic activity comparing to FH. A key limitation is the absence of non-parenchymal cells, such as stellate and endothelial cells, which are essential for maintaining hepatocyte function and drug metabolism [66]. For instance, the co-culture of HepaRG cells with stellate and/or endothelial cells has been shown to enhance extracellular matrix deposition and drug metabolism, making it a promising approach for drug screening applications [67]. Additionally, challenges related to nutrient supply and vascularization in long-term cultures impact metabolic function. Incorporating 3D-cultured hepatocytes with a perfusion system may improve oxygen and nutrient delivery, supporting long-term functionality and advancing the development of a more physiologically relevant hepatic model.

3.5. Inactivation of the YAP/TAZ pathway in the HCD model prevents dedifferentiation and prolongs hepatocyte function

To further elucidate that the bioprinted HCD model maintains PMH functions *in vitro*, we investigated the mechanical cues that regulate the Yes-associated protein (YAP)/transcriptional coactivator with PDZ-binding motif (TAZ) signaling pathway. Mechanical tension can induce stress fiber formation and subsequent YAP activation, leading to hepatocyte dedifferentiation [45]. Mechanoregulation of the *in vitro* culture is fundamentally different from the native *in vivo* microenvironment, significantly impacting cellular morphology and function in short-term cultures [68]. HCD is one main factor affecting the YAP/TAZ pathway, as it reduces the adhesive area and alters cell shape, leading to the inactivation of RhoA and a subsequent reduction in stress fibers within the actin cytoskeleton. This inactivation of YAP/TAZ occurs through both Hippo kinase-dependent and -independent mechanisms [69,70]. Our previous results have shown that cell-cell interactions are enabled in the HCD environment (Fig. 2), suggesting that these interactions could play a role in modulating YAP/TAZ activity (Fig. 4e).

Various mechanisms have been proposed to explain how cell-cell contact inhibition modulates YAP/TAZ activities and localization. First, in confluent cells, the adherens junction (AJ) protein E-cadherin *trans*-dimerizes, activating the MST1/2-LATS1/2 kinase cascade andinhibiting YAP/TAZ activity [71]. Second, the tight junction (TJ) protein ZO-1 forms between cells at high confluence, typically throughcis interactions of cell membrane proteins, which also contribute to YAP/TAZ inhibition [72]. Therefore, we hypothesized that the improved and prolonged hepatocyte function in HCD could be attributed to inactivated YAP/TAZ expression. To test this, we first evaluated the expression of AJ and TJ genes, specifically Cdh1 and Tjp1, respectively, using qRT-PCR (Fig. 4f). The expression of these genes was significantly increased in HCD, consistent with previous immunofluorescence staining and flow cytometry results (Fig. 2). Next, we employed RNA-seq to examine the YAP-related gene expression profiles in PMHs for both HCD and MCD. Heatmap analysis revealed that classic YAP-related genes were among those down-regulated in HCD (Fig. 4g). qRT-PCR results confirmed that the expression levels of *Yap1*, *Wwtr1* (TAZ), and their target genes *Ctgf* and *Cyr61* were all significantly lower in HCD (indicative of inactivation) compared to MCD (indicative of activation) (Fig. 4h). These findings demonstrate that the YAP/TAZ pathway is inactivated in HCD, suggesting that improved and prolonged hepatocyte functions in HCD are associated with the inactivation of the YAP/TAZ pathway. The increased cell-cell interactions and reduced mechanical stress in HCD contribute to this inactivation, providing a more physiologically relevant environment that supports primary hepatocyte function and viability. This mechanistic insight underscores the importance of cell density and mechanical cues in maintaining functional bioprinted liver models.

3.6. HCD liver models for drug screening

In vitro liver models are crucial for drug screening, especially during the early stages of drug development when numerous candidate compounds must be tested. These models need to be high throughput and capable of providing actionable data quickly, typically within 48 h. To address this need for drug screening applications, our bioprinted liver constructs were placed into a microfluidic chip, creating a dynamic culture system that more closely mimics the physiological environment. In addition to assessing the baseline CYP expression levels without any drug treatment, we examined the induction of specific CYP mRNA transcripts by treating the constructs with rifampicin (RIF), a bactericidal antibiotic known for its potential hepatotoxicity risks. The treatment with rifampicin resulted in significant increases in the expression of CYP3A4, CYP2C9, CYP2B6, and CYP1A2 in HCD, as illustrated in Fig. 5a. The expression of CYP3A4 and CYP2C9 genes was increased in both HCD and MCD. However, the CYP2B6 and CYP1A2 genes did not

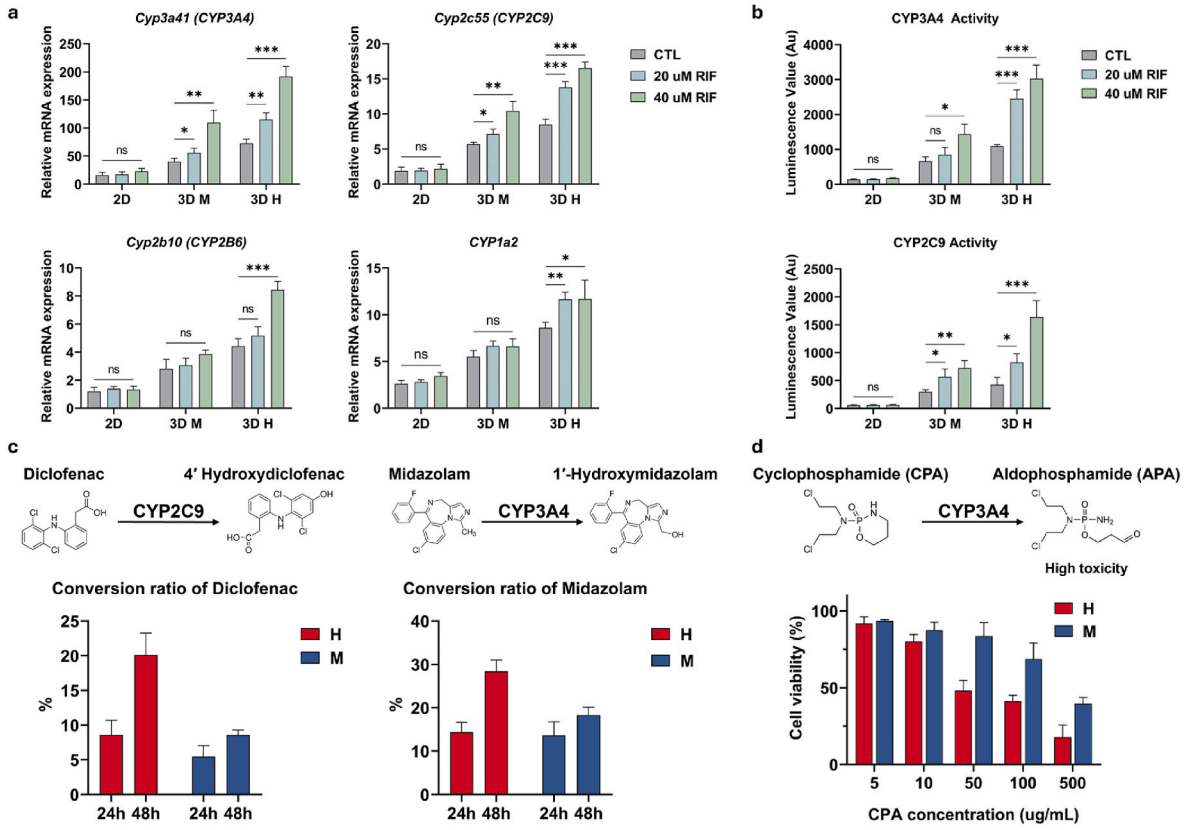

Fig. 5. HCD liver model for drug testing in a dynamic culture system. (a) Gene expression profiles showing levels of CYP3a41, CYP2c55, CYP2b10, and CYP1a2 in untreated (CTL) and rifampicin (RIF) treated samples on day 7 across three density conditions. Error bars represent SEM, and n = 3 was used for all data points. (b) CYP3A4 and CYP2C9 activity induction by RIF treatment across three density conditions. (c) The conversion ratio of diclofenac and midazolam metabolic products collected from cell culture medium after treating HCD and MCD constructs for 24 and 48 h. (d) Cytotoxicity analysis of CPA in the HCD and MCD liver models. Error bars represent mean ± s.d. *p < 0.05, **p < 0.01 and ***p < 0.001.

show significant upregulation in MCD. Additionally, the expression levels of these CYP genes in HCD were significantly elevated even at a lower concentration of rifampicin (20 μM), indicating that PMHs in HCD exhibit heightened sensitivity to this drug treatment. Similarly, the induction of CYP enzyme activity by rifampicin correlated with the observed gene expression patterns, providing further evidence that PMHs in HCD possess significant potential for drug screening applications (Fig. 5b).

To further evaluate the HCD liver construct's potential for metabolic drug conversion, diclofenac and midazolam were selected as model compounds due to their well-characterized metabolism by CYP enzymes. Diclofenac is primarily metabolized by CYP2C9, while midazolam is a substrate for CYP3A4. Monitoring the conversion rates of diclofenac and midazolam will guide the determination of an optimal therapeutic dose, ensuring drug efficacy while preventing toxic side effects during clinical use. After treatment with diclofenac and midazolam for 24 and 48 h, the drugs and their metabolites in the culture medium were quantified using mass spectrometry (MS). Multiple reaction monitoring (MRM) in negative ion mode was adopted to identify the target fragments, diclofenac (*m/z* 312.0) and its representative metabolite peaks 4-OH-diclofenac (*m/z* 230.0), as well as midazolam (*m/z* 342.0) and its representative metabolite peaks, 1-OH-Midazolam (*m/z* 203.0) (Table S1) [73]. Standard curves plotting concentration against representative fragment peak area were created using a series of diclofenac and midazolam standards (Fig. S11), and the concentrations of diclofenac and midazolam in the samples were calculated based on these linear relationships. The data indicated that MCD constructs exhibited a comparatively lower conversion rate than the HCD constructs (Fig. 5c). The higher conversion rates in HCD constructs suggest an enhanced metabolic capacity, likely due to the improved expression and functionality of CYP enzymes in the HCD environment. Cyclophosphamide (CPA), a widely used oxazaphosphorine prodrug, is easily absorbed but remains inactive until it is metabolized by mixed-function oxidase enzymes (cytochrome P450 system) in the liver. This metabolism yields phosphoramide mustard and acrolein, which alkylate DNA and proteins, respectively. To compare HCD and MCD models and demonstrate the superiority of the HCD model in drug screening, CPA concentrations ranging from 1 μg/mL to 500 μg/mL were employed for a drug toxicity test (Fig. 5d). The toxicity of CPA at MCD was relatively low, even at a concentration of 100 μg/mL, with no dose-dependent effects observed at lower drug concentrations (5–50 μg/mL). However, in the HCD model, cytotoxicity was shown to be concentration-dependent; as the drug concentration increased, increased cell death was observed. Drug toxicity results in static culture showed a similar dose-dependent profile in both HCD and MCD (Fig. S12). The IC50 results also indicated that the HCD liver model was useful and sensitive in evaluating cytotoxic reactions after the addition of the CPA (Table S2). Notably, after 24 h of CPA treatment, CYP3A4 expression in HCD cells was found to be dramatically higher than in MCD cells (Fig. S13). This observation suggests that the PMH in the HCD model successfully converted CPA to its active form, aldophosphamide, via the CYP3A4 enzyme. In addition, we included three additional clinically relevant compounds for drug screening: dexamethasone (a non-hepatotoxic drug serving as a control), acetaminophen (APAP), and voriconazole (both known as hepatotoxic agents) (Fig. S14). Our findings indicate that dexamethasone does not induce hepatotoxicity in either the HCD or MCD groups, consistent with clinical observations. In contrast, APAP and voriconazole exhibited increased toxicity in the HCD group, likely due to an elevated

production of toxic metabolites, thereby reinforcing the physiological relevance of our model. In comparison to clinical plasma concentrations (Cmax), our findings indicate that the IC50 values obtained in our model are higher than reported Cmax values for these drugs [74,75]. This discrepancy may stem from species-specific differences between primary human and mouse hepatocytes, as well as the absence of non-parenchymal liver cells in our current model. Although PMHs serve as a valuable model for investigating hepatic metabolism, enzyme activity, and drug-induced toxicity, species-specific differences in drug metabolism and cellular responses present a significant limitation, potentially reducing the translational applicability of PMHs in human drug safety assessments. In contrast, primary human hepatocytes (PHHs) are regarded as the gold standard for evaluating drug metabolism and toxicity, as they closely replicate human liver physiology and exhibit clinically relevant expression levels of key drug-metabolizing enzymes. Despite these advantages, the use of PHHs is constrained by challenges such as limited availability, donor-to-donor variability, and a rapid decline in viability and functionality under *in vitro* culture conditions. Therefore, we selected PMHs to validate our HCD printing strategy, despite differences in drug responses compared to human clinical testing. Additionally, *in vivo* hepatotoxic responses are influenced by interactions with endothelial cells, Kupffer cells, and stellate cells, which play crucial roles in drug metabolism, immune responses, and fibrosis progression. The absence of these supporting cell types in our system may affect drug sensitivity and toxicity thresholds. To enhance the translational relevance of our model and address these limitations, future studies will focus on bioprinting multicellular liver constructs that incorporate these additional cell types. This strategy is expected to facilitate a more comprehensive assessment of drug-induced hepatotoxicity and improve alignment with clinical pharmacokinetics.

4. Conclusion

We successfully fabricated an HCD liver model that maintains PMH function by incorporating iodixanol into a bioink. This approach enabled us to achieve both a high cell density ($\sim 8 \times 10^7$ cells/mL) and robust cell viability (~80 %). In the bioprinted HCD constructs, PMH cells formed cell aggregates and enhanced cell-cell interactions, as evidenced by increased expression of E-cadherin and ZO-1. This enabled the PHMs to sustain better metabolic functions including albumin secretion, urea production, and P450 metabolism. RNA-sequencing results indicated that LiGEP and xenobiotic metabolism-related genes are upregulated under HCD conditions. Furthermore, we investigated the mechanisms of YAP/TAZ pathway regulation in HCD and found that YAP/TAZ pathway-related genes were inactivated due to increased cell-cell interactions, which contribute to a more physiologically relevant liver environment. Finally, the HCD liver model demonstrated potential for drug screening applications due to its robust metabolic function, allowing it to sensitively detect toxicity at low drug concentrations.

CRediT authorship contribution statement

Ting-Yu Lu: Writing – review & editing, Writing – original draft, Visualization, Validation, Methodology, Investigation, Formal analysis, Data curation, Conceptualization. **Yichun Ji:** Data curation, Investigation, Methodology, Visualization, Writing – original draft, Writing – review & editing. **Cheng Lyu:** Writing – review & editing, Methodology, Investigation, Conceptualization. **Erin Nicole Shen:** Methodology, Investigation. **Yazhi Sun:** Methodology, Investigation. **Yi Xiang:** Methodology, Investigation. **Tobias Meng-Saccoccio:** Writing – review & editing. **Gen-Sheng Feng:** Writing – review & editing, Supervision, Conceptualization. **Shaochen Chen:** Writing – review & editing, Writing – original draft, Supervision, Project administration, Funding acquisition, Conceptualization.

Declaration of competing interest

The authors declare that they have no known competing financial interests or personal relationships that could have appeared to influence the work reported in this paper.

Acknowledgements

Funding: This work is supported in part by a grant (R21ES034455) from the National Institutes of Health and a grant from the National Science Foundation (2135720). We thank the UCSD School of Medicine Microscopy Core, which is supported by an NINDS P30 grant (NS047101), for the use of their confocal microscopes.

Appendix A. Supplementary data

Supplementary data to this article can be found online at https://doi.org/10.1016/j.biomaterials.2025.123256.

Data availability

Data will be made available on request.

References

[1] R.J. Andrade, N. Chalasani, E.S. Björnsson, A. Suzuki, G.A. Kullak-Ublick, P. B. Watkins, H. Devarbhavi, M. Merz, M.I. Lucena, N. Kaplowitz, Drug-induced liver injury, Nat. Rev. Dis. Primers 5 (1) (2019) 58.
[2] W.-C. Zhou, Q.-B. Zhang, L. Qiao, Pathogenesis of liver cirrhosis, World J. Gastroenterol.: WJG 20 (23) (2014) 7312.
[3] C. Guguen-Guillouzo, A. Guillouzo, General review on in vitro hepatocyte models and their applications. Hepatocytes: Methods and Protocols, 2010, pp. 1–40.
[4] H. Lee, W. Han, H. Kim, D.-H. Ha, J. Jang, B.S. Kim, D.-W. Cho, Development of liver decellularized extracellular matrix bioink for three-dimensional cell printing-based liver tissue engineering, Biomacromolecules 18 (4) (2017) 1229–1237.
[5] M.A. Tutty, D. Movia, A. Prina-Mello, Three-dimensional (3D) liver cell models-a tool for bridging the gap between animal studies and clinical trials when screening liver accumulation and toxicity of nanobiomaterials, Drug Delivery and Translational Research 12 (9) (2022) 2048–2074.
[6] G. Tuschl, B. Lauer, S.O. Mueller, Primary hepatocytes as a model to analyze species-specific toxicity and drug metabolism, Expet Opin. Drug Metabol. Toxicol. 4 (7) (2008) 855–870.
[7] I. Kaur, A. Vasudevan, P. Rawal, D.M. Tripathi, S. Ramakrishna, S. Kaur, S.K. Sarin, Primary hepatocyte isolation and cultures: technical aspects, challenges and advancements, Bioengineering 10 (2) (2023) 131.
[8] M. Ruoß, M. Vosough, A. Königsrainer, S. Nadalin, S. Wagner, S. Sajadian, D. Huber, Z. Heydari, S. Ehnert, J.G. Hengstler, Towards improved hepatocyte cultures: progress and limitations, Food Chem. Toxicol. 138 (2020) 111188.
[9] V.M. Lauschke, R.Z. Shafagh, D.F. Hendriks, M. Ingelman-Sundberg, 3D primary hepatocyte culture systems for analyses of liver diseases, drug metabolism, and toxicity: emerging culture paradigms and applications, Biotechnol. J. 14 (7) (2019) 1800347.
[10] P. Godoy, N.J. Hewitt, U. Albrecht, M.E. Andersen, N. Ansari, S. Bhattacharya, J. G. Bode, J. Bolleyn, C. Borner, J. Boettger, Recent advances in 2D and 3D in vitro systems using primary hepatocytes, alternative hepatocyte sources and non-parenchymal liver cells and their use in investigating mechanisms of hepatotoxicity, cell signaling and ADME, Arch. Toxicol. 87 (2013) 1315–1530.
[11] M.B. Esch, J.-M. Prot, Y.I. Wang, P. Miller, J.R. Llamas-Vidales, B.A. Naughton, D. R. Applegate, M.L. Shuler, Multi-cellular 3D human primary liver cell culture elevates metabolic activity under fluidic flow, Lab Chip 15 (10) (2015) 2269–2277.
[12] X. Ma, X. Qu, W. Zhu, Y.-S. Li, S. Yuan, H. Zhang, J. Liu, P. Wang, C.S.E. Lai, F. Zanella, Deterministically patterned biomimetic human iPSC-derived hepatic model via rapid 3D bioprinting, Proc. Natl. Acad. Sci. USA 113 (8) (2016) 2206–2211.
[13] J. Enderle, J. Bronzino, Introduction to Biomedical Engineering, Academic press, 2011.
[14] A.C. Daly, M.E. Prendergast, A.J. Hughes, J.A. Burdick, Bioprinting for the biologist, Cell 184 (1) (2021) 18–32.
[15] M.A. Skylar-Scott, S.G. Uzel, L.L. Nam, J.H. Ahrens, R.L. Truby, S. Damaraju, J. A. Lewis, Biomanufacturing of organ-specific tissues with high cellular density and embedded vascular channels, Sci. Adv. 5 (9) (2019) eaaw2459.
[16] B. Deng, Y. Ma, J. Huang, R. He, M. Luo, L. Mao, E. Zhang, Y. Zhao, X. Wang, Q. Wang, Revitalizing liver function in mice with liver failure through transplantation of 3D-bioprinted liver with expanded primary hepatocytes, Sci. Adv. 10 (23) (2024) eado1550.
[17] G. Janani, S. Priya, S. Dey, B.B. Mandal, Mimicking native liver lobule microarchitecture in vitro with parenchymal and non-parenchymal cells using 3D

bioprinting for drug toxicity and drug screening applications, ACS Appl. Mater. Interfaces 14 (8) (2022) 10167–10186.
[18] S. Maji, M. Lee, J. Lee, J. Lee, H. Lee, Development of lumen-based perfusable 3D liver in vitro model using single-step bioprinting with composite bioinks, Materials today bio 21 (2023) 100723.
[19] S. You, Y. Xiang, H.H. Hwang, D.B. Berry, W. Kiratitanaporn, J. Guan, E. Yao, M. Tang, Z. Zhong, X. Ma, High cell density and high-resolution 3D bioprinting for fabricating vascularized tissues, Sci. Adv. 9 (8) (2023) eade7923.
[20] Z. Zhang, Y. Jin, J. Yin, C. Xu, R. Xiong, K. Christensen, B.R. Ringeisen, D. B. Chrisey, Y. Huang, Evaluation of bioink printability for bioprinting applications, Appl. Phys. Rev. 5 (4) (2018).
[21] Y. Zhang, Y. He, S. Bharadwaj, N. Hammam, K. Carnagey, R. Myers, A. Atala, M. Van Dyke, Tissue-specific extracellular matrix coatings for the promotion of cell proliferation and maintenance of cell phenotype, Biomaterials 30 (23–24) (2009) 4021–4028.
[22] K.-C. Tang, K.-C. Yang, C.-W. Lin, Y.-K. Chen, T.-Y. Lu, H.-Y. Chen, N.-C. Cheng, J. Yu, Human adipose-derived stem cell secreted extracellular matrix incorporated into electrospun poly (lactic-co-glycolic acid) nanofibrous dressing for enhancing wound healing, Polymers 11 (10) (2019) 1609.
[23] C.-C. Tsai, S.-H. Kuo, T.-Y. Lu, N.-C. Cheng, M.-Y. Shie, J. Yu, Enzyme-cross-linked gelatin hydrogel enriched with an articular cartilage extracellular matrix and human adipose-derived stem cells for hyaline cartilage regeneration of rabbits, ACS Biomater. Sci. Eng. 6 (9) (2020) 5110–5119.
[24] Y. Fang, W. Sun, T. Zhang, Z. Xiong, Recent advances on bioengineering approaches for fabrication of functional engineered cardiac pumps: a review, Biomaterials 280 (2022) 121298.
[25] E.N. Farah, R.K. Hu, C. Kern, Q. Zhang, T.-Y. Lu, Q. Ma, S. Tran, B. Zhang, D. Carlin, A. Monell, Spatially organized cellular communities form the developing human heart, Nature 627 (8005) (2024) 854–864.
[26] Y. Xiang, K. Miller, J. Guan, W. Kiratitanaporn, M. Tang, S. Chen, 3D bioprinting of complex tissues in vitro: state-of-the-art and future perspectives, Arch. Toxicol. 96 (3) (2022) 691–710.
[27] S. You, J. Li, W. Zhu, C. Yu, D. Mei, S. Chen, Nanoscale 3D printing of hydrogels for cellular tissue engineering, J. Mater. Chem. B 6 (15) (2018) 2187–2197.
[28] M. Tang, S.K. Tiwari, K. Agrawal, M. Tan, J. Dang, T. Tam, J. Tian, X. Wan, J. Schimelman, S. You, Rapid 3D bioprinting of glioblastoma model mimicking native biophysical heterogeneity, Small 17 (15) (2021) 2006050.
[29] J. Ren, P. Han, X. Ma, E.N. Farah, J. Bloomekatz, X.-X.I. Zeng, R. Zhang, M. M. Swim, A.D. Witty, H.G. Knight, Canonical Wnt5b signaling directs outlying Nkx2. 5+ mesoderm into pacemaker cardiomyocytes, Dev. Cell 50 (6) (2019) 729, 743. e5.
[30] T.-Y. Lu, Y. Xiang, M. Tang, S. Chen, 3D printing approaches to engineer cardiac tissue, Curr. Cardiol. Rep. 25 (6) (2023) 505–514.
[31] S. Boularaoui, G. Al Hussein, K.A. Khan, N. Christoforou, C. Stefanini, An overview of extrusion-based bioprinting with a focus on induced shear stress and its effect on cell viability, Bioprinting 20 (2020) e00093.
[32] J. He, J. Wang, Y. Pang, H. Yu, X. Qin, K. Su, T. Xu, H. Ren, Bioprinting of a hepatic tissue model using human-induced pluripotent stem cell-derived hepatocytes for drug-induced hepatotoxicity evaluation, International Journal of Bioprinting 8 (3) (2022).
[33] D.A. Kukla, A.L. Crampton, D.K. Wood, S.R. Khetani, Microscale collagen and fibroblast interactions enhance primary human hepatocyte functions in three-dimensional models, Gene Expr. 20 (1) (2020) 1.
[34] Q. Mao, Y. Wang, Y. Li, S. Juengpanich, W. Li, M. Chen, J. Yin, J. Fu, X. Cai, Fabrication of liver microtissue with liver decellularized extracellular matrix (dECM) bioink by digital light processing (DLP) bioprinting, Mater. Sci. Eng. C 109 (2020) 110625.
[35] L. Sun, Y. Wang, S. Zhang, H. Yang, Y. Mao, 3D bioprinted liver tissue and disease models: current advances and future perspectives, Biomater. Adv. 152 (2023) 213499.
[36] T.-Y. Lu, K.-F. Yu, S.-H. Kuo, N.-C. Cheng, E.-Y. Chuang, J.-S. Yu, Enzyme-crosslinked gelatin hydrogel with adipose-derived stem cell spheroid facilitating wound repair in the murine burn model, Polymers 12 (12) (2020) 2997.
[37] M. Cuvellier, S. Rose, F. Ezan, U. Jarry, H. de Oliveira, A. Bruyère, C.D. La Rochelle, V. Legagneux, S. Langouët, G. Baffet, In vitro long term differentiation and functionality of three-dimensional bioprinted primary human hepatocytes: application for in vivo engraftment, Biofabrication 14 (3) (2022) 035021.
[38] S. Jeon, J.H. Heo, M.K. Kim, W. Jeong, H.W. Kang, High-precision 3D bio-dot printing to improve paracrine interaction between multiple types of cell spheroids, Adv. Funct. Mater. 30 (52) (2020) 2005324.
[39] M.K. Kim, W. Jeong, S. Jeon, H.-W. Kang, 3D bioprinting of dECM-incorporated hepatocyte spheroid for simultaneous promotion of cell-cell and-ECM interactions, Front. Bioeng. Biotechnol. 11 (2023).
[40] I.T. Ozbolat, M. Hospodiuk, Current advances and future perspectives in extrusion-based bioprinting, Biomaterials 76 (2016) 321–343.
[41] X. Jiang, J. Xu, J.C. Gore, Mapping hepatocyte size in vivo using temporal diffusion spectroscopy MRI, Magn. Reson. Med. 84 (5) (2020) 2671–2683.
[42] A.C. Daly, M.D. Davidson, J.A. Burdick, 3D bioprinting of high cell-density heterogeneous tissue models through spheroid fusion within self-healing hydrogels, Nat. Commun. 12 (1) (2021) 753.
[43] B. Grigoryan, S.J. Paulsen, D.C. Corbett, D.W. Sazer, C.L. Fortin, A.J. Zaita, P. T. Greenfield, N.J. Calafat, J.P. Gounley, A.H. Ta, Multivascular networks and functional intravascular topologies within biocompatible hydrogels, Science 364 (6439) (2019) 458–464.
[44] J. Guan, S. You, Y. Xiang, J. Schimelman, J. Alido, X. Ma, M. Tang, S. Chen, Compensating the cell-induced light scattering effect in light-based bioprinting using deep learning, Biofabrication 14 (1) (2021) 015011.
[45] P. Sun, G. Zhang, X. Su, C. Jin, B. Yu, X. Yu, Z. Lv, H. Ma, M. Zhang, W. Wei, Maintenance of primary hepatocyte functions in vitro by inhibiting mechanical tension-induced YAP activation, Cell Rep. 29 (10) (2019) 3212, 3222. e4.
[46] K.L. Miller, I. Sit, Y. Xiang, J. Wu, J. Pustelnik, M. Tang, W. Kiratitanaporn, V. Grassian, S. Chen, Evaluation of CuO nanoparticle toxicity on 3D bioprinted human iPSC-derived cardiac tissues, Bioprinting 32 (2023) e00284.
[47] X. Ma, C. Yu, P. Wang, W. Xu, X. Wan, C.S.E. Lai, J. Liu, A. Koroleva-Maharajh, S. Chen, Rapid 3D bioprinting of decellularized extracellular matrix with regionally varied mechanical properties and biomimetic microarchitecture, Biomaterials 185 (2018) 310–321.
[48] P. Soman, B.T. Tobe, J.W. Lee, A.A. Winquist, I. Singec, K.S. Vecchio, E.Y. Snyder, S. Chen, Three-dimensional scaffolding to investigate neuronal derivatives of human embryonic stem cells, Biomedical microdevices 14 (2012) 829–838.
[49] K.L. Miller, Y. Xiang, C. Yu, J. Pustelnik, J. Wu, X. Ma, T. Matsui, K. Imahashi, S. Chen, Rapid 3D BioPrinting of a human iPSC-derived cardiac micro-tissue for high-throughput drug testing, Organs-on-a-Chip 3 (2021) 100007.
[50] Y. Sun, X. Wang, M. Tang, M.K. Melarkey, T.y. Lu, Y. Xiang, S. Chen, 3D printing of succulent-inspired microneedle array for enhanced tissue adhesion and controllable drug release, Advanced Materials Technologies (2024) 2400216.
[51] W. Kiratitanaporn, J. Guan, M. Tang, Y. Xiang, T.-y. Lu, A. Balayan, A. Lao, D. B. Berry, S. Chen, 3D printing of a biomimetic myotendinous junction assisted by artificial intelligence, Biomater. Sci. 12 (23) (2024) 6047–6062.
[52] J. Liu, J. He, J. Liu, X. Ma, Q. Chen, N. Lawrence, W. Zhu, Y. Xu, S. Chen, Rapid 3D bioprinting of in vitro cardiac tissue models using human embryonic stem cell-derived cardiomyocytes, Bioprinting 13 (2019) e00040.
[53] P. Sang-Hyun, W. Pengrui, Z. Wei, W. John, C. Shaochen, Continuous Optical 3D Printing of Green Aliphatic Polyurethanes, 2017.
[54] D. Tang, M. Chen, X. Huang, G. Zhang, L. Zeng, G. Zhang, S. Wu, Y. Wang, SRplot: a free online platform for data visualization and graphing, PLoS One 18 (11) (2023) e0294236.
[55] T. Boothe, L. Hilbert, M. Heide, L. Berninger, W.B. Huttner, V. Zaburdaev, N. L. Vastenhouw, E.W. Myers, D.N. Drechsel, J.C. Rink, A tunable refractive index matching medium for live imaging cells, tissues and model organisms, Elife 6 (2017) e27240.
[56] W. Choi, C. Fang-Yen, K. Badizadegan, S. Oh, N. Lue, R.R. Dasari, M.S. Feld, Tomographic phase microscopy, Nat. Methods 4 (9) (2007) 717–719.
[57] P.N. Bernal, M. Bouwmeester, J. Madrid-Wolff, M. Falandt, S. Florczak, N. G. Rodriguez, Y. Li, G. Größbacher, R.A. Samsom, M. van Wolferen, Volumetric bioprinting of organoids and optically tuned hydrogels to build liver-like metabolic biofactories, Adv. Mater. 34 (15) (2022) 2110054.
[58] J. You, S.-A. Park, D.-S. Shin, D. Patel, V.K. Raghunathan, M. Kim, C.J. Murphy, G. Tae, A. Revzin, Characterizing the effects of heparin gel stiffness on function of primary hepatocytes, Tissue Eng. 19 (23–24) (2013) 2655–2663.
[59] T.T. Chang, M. Hughes-Fulford, Molecular mechanisms underlying the enhanced functions of three-dimensional hepatocyte aggregates, Biomaterials 35 (7) (2014) 2162–2171.
[60] K.P. Kanebratt, A. Janefeldt, L. Vilén, A. Vildhede, K. Samuelsson, L. Milton, A. Björkbom, M. Persson, C. Leandersson, T.B. Andersson, Primary human hepatocyte spheroid model as a 3D in vitro platform for metabolism studies, J. Pharmaceut. Sci. 110 (1) (2021) 422–431.
[61] C.C. Bell, D.F. Hendriks, S.M. Moro, E. Ellis, J. Walsh, A. Renblom, L. Fredriksson Puigvert, A.C. Dankers, F. Jacobs, J. Snoeys, Characterization of primary human hepatocyte spheroids as a model system for drug-induced liver injury, liver function and disease, Sci. Rep. 6 (1) (2016) 25187.
[62] J.L. Luebke-Wheeler, G. Nedredal, L. Yee, B.P. Amiot, S.L. Nyberg, E-cadherin protects primary hepatocyte spheroids from cell death by a caspase-independent mechanism, Cell Transplant. 18 (12) (2009) 1281–1287.
[63] D.S. Kim, J.W. Ryu, M.Y. Son, J.H. Oh, K.S. Chung, S. Lee, J.J. Lee, J.H. Ahn, J. S. Min, J. Ahn, A liver-specific gene expression panel predicts the differentiation status of in vitro hepatocyte models, Hepatology 66 (5) (2017) 1662–1674.
[64] S.-F. Zhou, J.-P. Liu, B. Chowbay, Polymorphism of human cytochrome P450 enzymes and its clinical impact, Drug Metab. Rev. 41 (2) (2009) 89–295.
[65] F.P. Guengerich, Cytochrome P-450 3A4: regulation and role in drug metabolism, Annu. Rev. Pharmacol. Toxicol. 39 (1) (1999) 1–17.
[66] Y. Koui, T. Kido, T. Ito, H. Oyama, S.-W. Chen, Y. Katou, K. Shirahige, A. Miyajima, An in vitro human liver model by iPSC-derived parenchymal and non-parenchymal cells, Stem Cell Rep. 9 (2) (2017) 490–498.
[67] M. Cuvellier, F. Ezan, H. Oliveira, S. Rose, J.-C. Fricain, S. Langouët, V. Legagneux, G. Baffet, 3D culture of HepaRG cells in GelMa and its application to bioprinting of a multicellular hepatic model, Biomaterials 269 (2021) 120611.
[68] L. Chang, L. Azzolin, D. Di Biagio, F. Zanconato, G. Battilana, R. Lucon Xiccato, M. Aragona, S. Giulitti, T. Panciera, A. Gandin, The SWI/SNF complex is a mechanoregulated inhibitor of YAP and TAZ, Nature 563 (7730) (2018) 265–269.
[69] M. Aragona, T. Panciera, A. Manfrin, S. Giulitti, F. Michielin, N. Elvassore, S. Dupont, S. Piccolo, A mechanical checkpoint controls multicellular growth through YAP/TAZ regulation by actin-processing factors, Cell 154 (5) (2013) 1047–1059.
[70] Z. Meng, T. Moroishi, K.-L. Guan, Mechanisms of Hippo pathway regulation, Genes & development 30 (1) (2016) 1–17.
[71] N.-G. Kim, E. Koh, X. Chen, B.M. Gumbiner, E-cadherin mediates contact inhibition of proliferation through Hippo signaling-pathway components, Proc. Natl. Acad. Sci. USA 108 (29) (2011) 11930–11935.

[72] Y. Li, H. Zhou, F. Li, S.W. Chan, Z. Lin, Z. Wei, Z. Yang, F. Guo, C.J. Lim, W. Xing, Angiomotin binding-induced activation of Merlin/NF2 in the Hippo pathway, Cell Res. 25 (7) (2015) 801–817.
[73] B. Scheidecker, S. Poulain, M. Sugimoto, T. Kido, T. Kawanishi, A. Miyajima, S. H. Kim, H. Arakawa, Y. Kato, M. Nishikawa, Dynamic, IPSC-derived hepatic tissue tri-culture system for the evaluation of liver physiology in vitro, Biofabrication 16 (2) (2024) 025037.
[74] H.M. Lazarus, J.L. Blumer, S. Yanovich, H. Schlamm, A. Romero, Safety and pharmacokinetics of oral voriconazole in patients at risk of fungal infection: a dose escalation study, J. Clin. Pharmacol. 42 (4) (2002) 395–402.
[75] L.P. James, L. Letzig, P.M. Simpson, E. Capparelli, D.W. Roberts, J.A. Hinson, T. J. Davern, W.M. Lee, Pharmacokinetics of acetaminophen-protein adducts in adults with acetaminophen overdose and acute liver failure, Drug Metabol. Dispos. 37 (8) (2009) 1779–1784.